APL Materials

Enhanced electroresistance endurance of capped $Hf_{0.5}Zr_{0.5}O_2$ ultrathin epitaxial tunnel barriers

Cite as: APL Mater. **10**, 031114 (2022); https://doi.org/10.1063/5.0076865
Submitted: 28 October 2021 • Accepted: 03 March 2022 • Published Online: 23 March 2022

Xiao Long, Huan Tan, Saúl Estandía, et al.

COLLECTIONS

Paper published as part of the special topic on Materials Challenges for Nonvolatile Memory

ARTICLES YOU MAY BE INTERESTED IN

Impact of non-ferroelectric phases on switching dynamics in epitaxial ferroelectric $Hf_{0.5}Zr_{0.5}O_2$ films
APL Materials **10**, 031108 (2022); https://doi.org/10.1063/5.0083661

Atomic layer etching of ferroelectric hafnium zirconium oxide thin films enables giant tunneling electroresistance
Applied Physics Letters **120**, 122901 (2022); https://doi.org/10.1063/5.0084636

Ferroelectricity in hafnium oxide thin films
Applied Physics Letters **99**, 102903 (2011); https://doi.org/10.1063/1.3634052

© 2022 Author(s).

Enhanced electroresistance endurance of capped $Hf_{0.5}Zr_{0.5}O_2$ ultrathin epitaxial tunnel barriers

Cite as: APL Mater. 10, 031114 (2022); doi: 10.1063/5.0076865
Submitted: 28 October 2021 • Accepted: 3 March 2022 •
Published Online: 23 March 2022

View Online
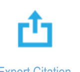
Export Citation

CrossMark

Xiao Long, Huan Tan, Saúl Estandía, Jaume Gazquez, Florencio Sánchez, Ignasi Fina,[a] and Josep Fontcuberta[a]

AFFILIATIONS

Institut de Ciència de Materials de Barcelona (ICMAB-CSIC), Campus UAB, Bellaterra, Catalonia 08193, Spain

Note: This paper is part of the Special Topic on Materials Challenges for Nonvolatile Memory.
[a]**Authors to whom correspondence should be addressed:** ifina@icmab.es and fontcuberta@icmab.cat

ABSTRACT

Electroresistance in ultrathin $Hf_{0.5}Zr_{0.5}O_2$ (HZO) films is pivotal toward the implementation of hafnia-based ferroelectrics in electronics. Here, we show that the electroresistance yield and endurance of large capacitors (~314 μm^2) of epitaxial HZO films only 2.2 nm thick grown on $SrTiO_3$ or $GdScO_3$ can be improved using 1 nm $SrTiO_3$ capping layers. It is argued that the main role of the capping layer is to minimize charge transport along grain boundaries, and, thus, a similar strategy can be explored in polycrystalline films.

© *2022 Author(s). All article content, except where otherwise noted, is licensed under a Creative Commons Attribution (CC BY) license (http://creativecommons.org/licenses/by/4.0/).* https://doi.org/10.1063/5.0076865

INTRODUCTION

Achieving robust electroresistance (ER) response and good endurance and retention while reducing the spread of ER values in different devices on a wafer are prerequisites for the implementation of ferroelectric HfO_2-based tunnel barriers in data storage and computing architectures. Doping HfO_2 is typically required to obtain the ferroelectric orthorhombic phase (o-phase), and probably, $Hf_{0.5}Zr_{0.5}O_2$ (HZO) is the most studied composition.[1,2] In contrast to common ferroelectrics, ferroelectricity in doped HfO_2 films is known to be more prominent when reducing the film thickness.[3] It has been proposed that this uncommon behavior results from the fact that the metastable orthorhombic (o-)phase emerges as a result of competing bulk and interface contributions to the stabilization energy,[4] although recent reports showing the tremendous impact of the nature of the electrodes on the stabilization of the o-phase in epitaxial films suggest that the understanding of the interface energy contribution is far from complete.[5]

The presence of grain boundaries (GBs) in HZO has a detrimental effect on the device performance. Indeed, it has been shown that grain boundaries in polycrystalline films offer conducting paths for a charge motion[6] that may mask or even preclude a genuine intrinsic electroresistance associated with ferroelectric polarization switching.[7] Similarly, in epitaxial HZO films grown on single crystalline substrates, the presence of twins of the orthorhombic phase or the presence of different HZO polymorphs in the film creates a network of grain boundaries that are the source of conducting channels. These conducting channels open at some voltage and induce a non-ferroelectric ER that perturbs device performance.[6,8–13] Interestingly, it has been shown that the relative amount of the different polymorphs of HZO is determined by the substrate selection.[14] For instance, HZO films only a few nanometers thick (5–10 nm) grown on $SrTiO_3$ (STO) typically contain the monoclinic (m-) and the o-phases and the corresponding twined crystals. In contrast, films grown on scandates, for instance, $GdScO_3$ (GSO), display almost exclusively the twinned o-phase. It, thus, follows that grain boundaries and subsequently spurious conducting channels are more prevalent in HZO films grown on STO than on GSO, the latter displaying a more robust ER response.[15] Sulzbach *et al.*[16] have shown that a way to mitigate the role of grain boundaries on the ER is to use a dielectric layer as a capping of the epitaxial film. By exploring the ER of HZO films of 4.5 nm grown on STO and GSO and capped with an ultrathin layer (≈1 nm) of STO or AlO_x, it was possible to largely increase the yield of tunnel barriers on a wafer, and importantly, the spread of ER values was reduced and the endurance was largely improved. In addition, in the quest toward ultrathin functional ferroelectric HZO epitaxial films, it has been shown[17] that

© Author(s) 2022

spike-timing-dependent plasticity (STDP) is found in ferroelectric HZO epitaxial thin films of only 2 nm-thick. Therefore, the natural next step is to explore to what extent dielectric capping of ultrathin HZO barriers could also be effective in improving yield, homogeneous resistance, and enhanced endurance as discovered earlier in thicker films, which would have the added benefit of a relatively reduced device resistance.

Here, it will be shown that capping an ultrathin ferroelectric HZO film (≈2 nm) grown on STO and GSO with 1 nm of STO definitely leads to more robust ferroelectric tunnel junctions, where ER displays a larger endurance and higher yield. X-ray photoelectron spectroscopy (XPS) and scanning transition electron microscopy data were used to obtain insights into the mechanisms leading to the higher performance of capped devices. It is argued that the primary role of the capping layer is to block conducting channels across grain boundaries.

EXPERIMENTAL

Epitaxial HZO films of 2.2 nm nominal thickness were grown on $SrTiO_3$ (001)-oriented (STO) and $GdScO_3$ (001)-oriented (GSO) (using pseudo-cubic setting) single crystalline substrates (5×5 mm^2) buffered with $La_{2/3}Sr_{1/3}MnO_3$ (LSMO, 22 nm thick) conducting electrodes by pulsed laser deposition (PLD), as described elsewhere.[18] HZO was subsequently capped with a STO layer deposited by ablating a $SrTiO_3$ target at $P(O_2) = 0.02$ mbar and T = 700 °C and cooled to room temperature under $P(O_2) = 0.2$ mbar. The thickness (t) of the STO capping layer was chosen to be $t \approx 1$ nm as controlled by the number of laser pulses on the basis of calibrated growth rates previously determined. Circular Pt top electrodes of 20 μm of diameter and 20 nm of thickness were grown at room temperature through shadow masks by sputtering. The junction structure of bare and capped samples is sketched in Figs. 1(a)–1(c). The reference sample, i.e., in which no dielectric material was deposited between the HZO layer and Pt, is labeled HZO. Films grown on STO and GSO substrates are labeled STO//HZO and GSO//HZO. Ferroelectric characterization by the piezoelectric force microscopy technique of samples grown on STO is shown in the supplementary material, S1. Samples grown on GSO have been characterized in detail elsewhere.[17] The samples with STO capping (1 nm) are named STO//HZO/STO1 and GSO//HZO/STO1.

Electric measurements were performed by contacting the bottom electrode LSMO and one top Pt electrode. All electrical characterization were performed using the TFAnalyser2000 platform (aixACCT Systems GmbH). The resistance is measured after each writing pulses (V_w) and after a delay time $\tau_D = 1$ s by applying a linear $V_R(t)$ triangular pulse of 1 s duration in a small voltage range (from −0.5 to +0.5 V). The resistance is calculated at $V_R = 0.5$ V. The V_w pulse is applied using a trapezoidal signal with the duration τ_w. Further details are described elsewhere.[17] The electric cycling of the junctions (named training in this work) was carried out using bipolar square pulses of indicated number ($N_C = 10^4$ times) at 5 kHz and 2.5 V amplitude.

X-ray photoelectron spectroscopy (XPS) was performed in ultrahigh vacuum of 5×10^{-10} mbar with a SPECS Phoibos 150 hemispherical analyzer using monochromatic Al Kα radiation with an energy of 1486.6 eV. To explore the depth dependence of the XPS data, the emission angle was chosen to be 0°, 45°, and 60°, with respect to the normal to the sample surface. Samples were in contact with air when transferred from the PLD chamber to the UHV XPS chamber. Energy calibration was carried out by fixing the energy of the Pt line. The deconvolution of the Hf and Ti core level spectra

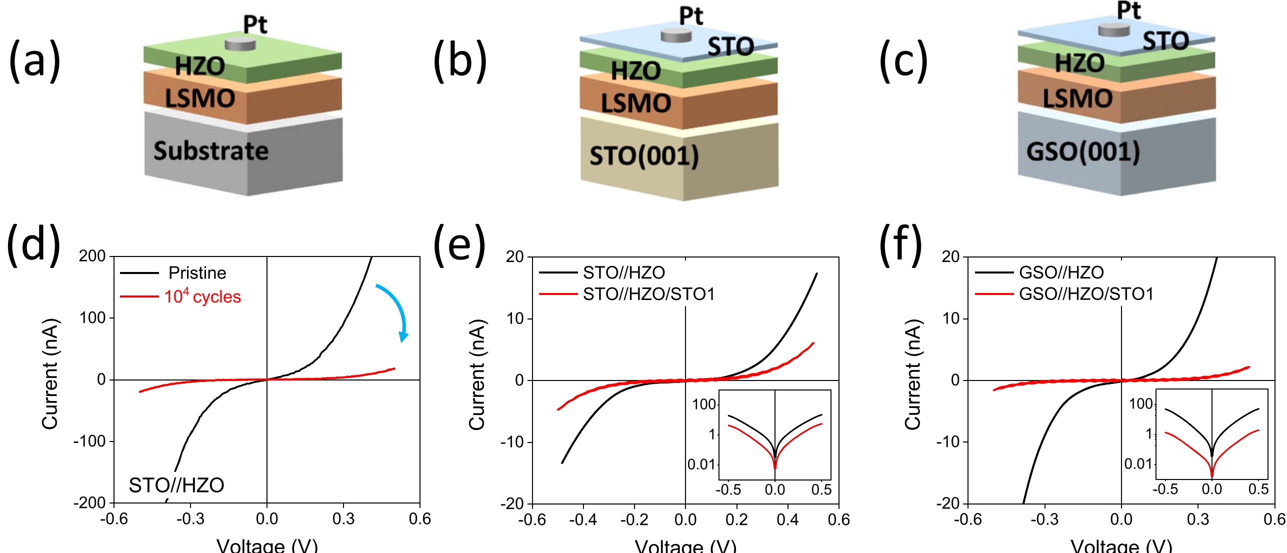

FIG. 1. (a)–(c) Sketches of the junction structure without/with dielectric capping. (d) Illustrative example of the training effect. The I–V characteristics before/after training in the STO//HZO sample. (e) and (f) I–V characteristics of STO//HZO and STO//HZO/STO1 and GSO//HZO and GSO//HZO/STO1 substrates, respectively. Data shown in panels (e) and (f) have been collected in trained devices. The insets in (e) and (f) display data in the semi-log scale.

© Author(s) 2022

was performed using the CasaXPS software, and backgrounds were subtracted using a Shirley type function.

Scanning transmission electron microscopy characterization: Aberration-corrected scanning transmission electron microscopy (STEM) was used for microstructural analysis with atomic resolution. The HZO film with 1 nm STO capping was characterized using a JEOL JEM-ARM200CF operated at 200 kV, equipped with a CEOS GmbH aberration corrector and a GIF Quantum ER spectrometer, at the University Complutense of Madrid, Spain. The STEM images were acquired in a high angle annular dark field (HAADF) imaging mode, also referred to as Z-contrast because the brightness associated with each atomic column roughly scales with the square of the atomic number Z.[19] The electron energy loss spectroscopy (EELS) chemical maps were obtained by integrating the characteristic edges of each element at each location. The STEM specimens were prepared using a FEI Helios NanoLab 650.

RESULTS

The I–V curves collected from pristine junctions in STO//HZO and after training cycles are shown in Fig. 1(d). It can be observed [insets in Fig. 1(d)] that in agreement with earlier reports,[17] the resistance increases after voltage training. A similar trend is observed in the STO//HZO/STO1 capped samples (see the supplementary material, S2), and a less perceptible resistance increase is observed in the GSO//HZO and GSO//HZO/STO1 films (see the supplementary material, S3). Of higher interest here is the impact of the capping layer on the junction resistance. In Figs. 1(e) and 1(f) (main panels and insets), we show the I–V curves collected on trained STO//HZO, STO//HZO/STO1, and GSO//HZO/STO1 samples. It can be readily appreciated that irrespective of the substrate, the resistance after the training is larger in the capped samples (STO//HZO/STO1 and GSO//HZO/STO1) than in the bare (STO, GSO)//HZO samples, which is consistent with the dielectric nature of the thin STO capping layer.

Different resistance states can we written on the junctions by applying writing voltage pulses of different amplitude and polarity. In Fig. 2(a), we show the data obtained from STO//HZO (black symbols) and STO//HZO/STO1 (red symbols) devices, electrically written with V_W up to ±20 V and using τ_W = 100 μs. It can be appreciated in Fig. 2(a) that a sharp drop of resistance occurs for STO//HZO at some critical writing voltage ($V_{W,C}$ ≈ 10 V). A similar behavior had been reported earlier in thicker HZO (≈4.5 nm) films grown on STO, and it was attributed to a voltage threshold between the polarization-controlled resistance and ionic motion.[15] Obviously, the capped STO//HZO/STO1 (red symbols) sample displays a larger resistance than the uncapped sample. Contrasting with the observations in relatively thicker HZO films (4.5 nm), in this ultrathin HZO barriers, the capping layer does not produce any perceptible increase in $V_{W,C}$.[16] On the other hand, the resistance of GSO//HZO remains robust at least up to V_W 20 V [Fig. 2(b)], which is in agreement with the claim that HZO films on GSO substrates have a reduced density of grain boundaries. In addition, the STO capping (GSO//HZO/STO1) increases the overall resistance of the junction.

Figures 3(a) and 3(b) display the ER R(V_w) loops collected on trained STO//HZO and STO//HZO/STO1 samples, with $-V_{max} < V_w < V_{max}$, with V_{max} = 2.5 V and V_{max} = 5 V , respectively, and writing times τ_w = 100 μs. Obvious ON/OFF (low resistance/high resistance, LRS/HRS) states develop at about V_W ≈ 2.5 V in all samples. Several relevant observations can be made from the data in Figs. 3(a) and 3(b): (a) the electroresistance increases with the writing voltage and (b) the insertion of the STO capping layer produces an obvious increase in the junction resistance. As inferred from the data in Figs. 3(a) and 3(b), the ER values range from 112% (STO//HZO) to 183% (STO//HZO/STO1). Ambriz-Vargas *et al.* measured the electroresistance of HZO barriers of similar thickness sandwiched between TiN and Pt. These authors reported ER values as large as 1500%.[20,21] However, the resistance of the junctions[20] was intriguingly smaller by some orders of magnitude than in the present case, challenging understanding and comparison. Recent results obtained in epitaxial films, similarly grown on LSMO and using Pt as top electrodes, show similar resistance values.[22] In polycrystalline HZO, resistance values as large as those measured in epitaxial films are only observed in thicker films.[23] This is consistent with the claimed contribution of grain boundaries to electrical transport.

Figures 3(c) and 3(d) show the electroresistance of GSO//HZO and GSO//HZO/STO1 samples. It can be appreciated that the impact of the writing voltage is similar to that observed for HZO on STO substrates [Figs. 3(a) and 3(b)]. However, it is apparent that the beneficial role of the STO capping is less perceptible. This observation suggests that the STO capping layer has a major impact on

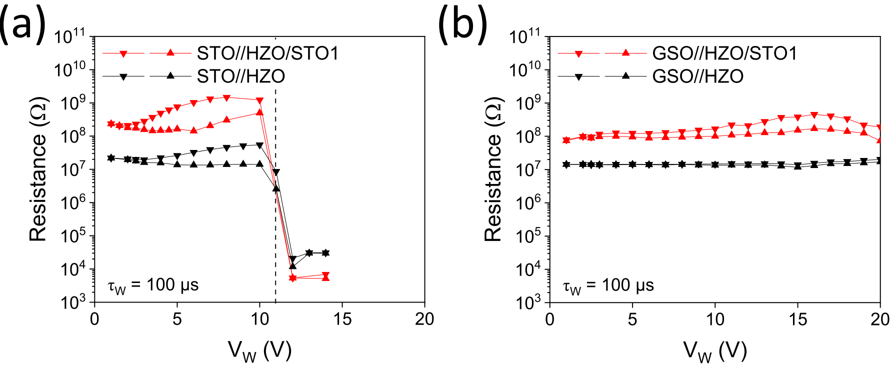

FIG. 2. (a) and (b) Resistance vs writing voltage (V_W) of bare and capped HZO samples grown on STO and GSO substrates, respectively. Up/down symbols indicate positive/negative writing voltages, respectively.

© Author(s) 2022

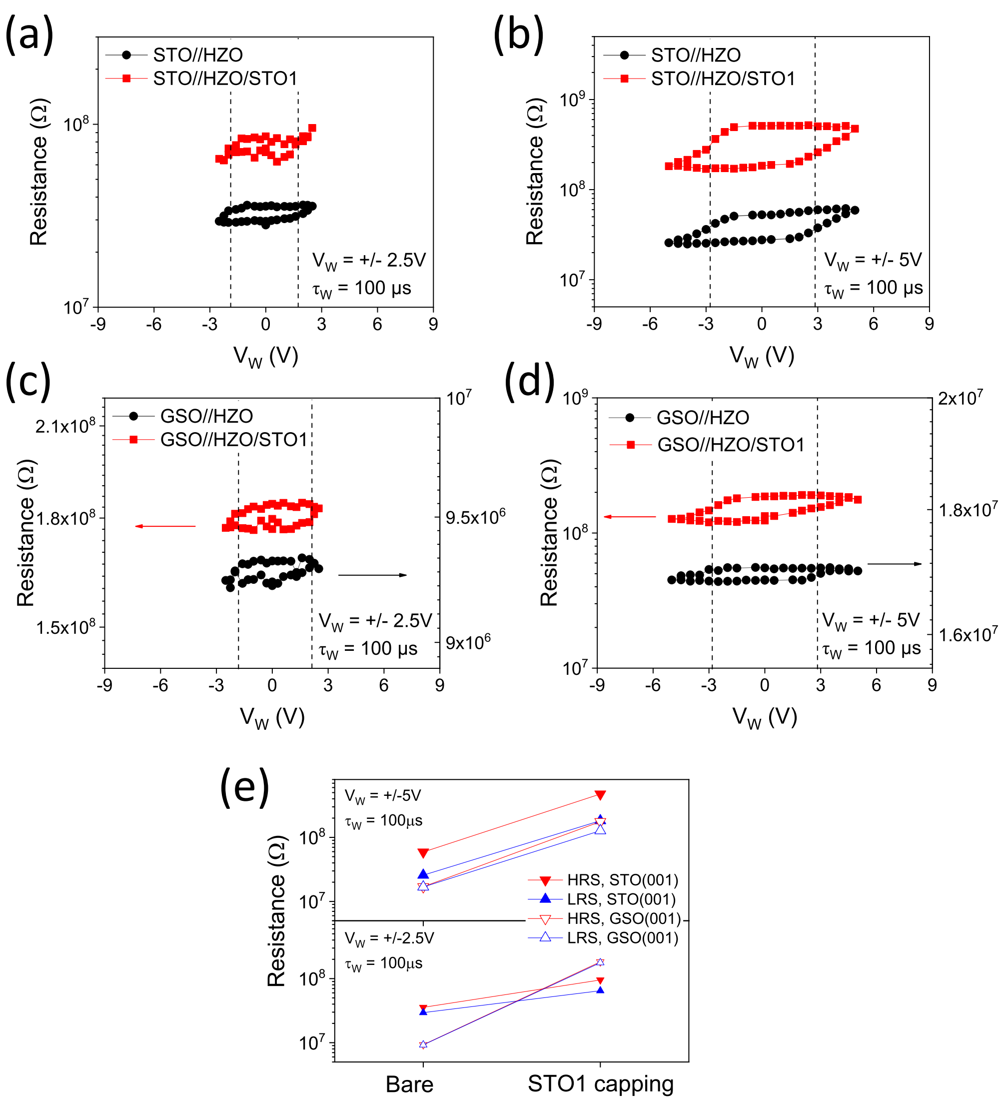

FIG. 3. Electroresistance of HZO and HZO/STO1 grown on (a) and (b) STO and (c) and (d) GSO, electrically written with V_{max} = 2.5 V (a) and (c) and V_{max} = 5 V (b) and (d), respectively. (e) Comparison of LRS and HRS states obtained after V_w writing of bare and capped samples.

the charge transport along grain boundaries which are more abundant in STO//HZO than in GSO//HZO. Note that GSO//HZO shows smaller resistance (9.3–17 MΩ) and electroresistance (0.8%–1.2%) than similar samples reported elsewhere,[17] probably due to the strong thickness dependence of tunneling current and small differences on the samples' thickness. Data reported above show that STO capping of both STO//HZO and GSO//HZO samples increases the overall device resistance as summarized in Fig. 3(e), where LRS and HRS for samples with and without the capping layer grown on both STO and GSO substrates are shown.

Next, we turn to inspect the role of the capping layer on the variability of ER from junction to junction (up to 15 junctions have been measured) on the same sample. Raw data of ON and OFF (LRS and HRS) resistance states written on junctions on bare STO//HZO and on STO//HZO/STO1, respectively, are included in the supplementary material, S4. The most illustrative results are depicted in Figs. 4(a) and 4(b) where we show the distribution R_N/R_{mean} of the recorded values, where R_{mean} is the mean value of the resistance distribution $\{R_N\}$ for STO/HZO and STO//HZO/STO1. The data clearly show that capping with the STO dielectric allows us to reduce the spread of resistance values of the tunnel junctions in the device. Note that ER has been measured with the contact tip directly placed onto the electrodes. Therefore, it cannot be excluded that the observed higher reproducibility of the resistance states in the capped devices might also be affected by the different mechanical stabilities of the capped device. Simultaneously, the endurance

© Author(s) 2022

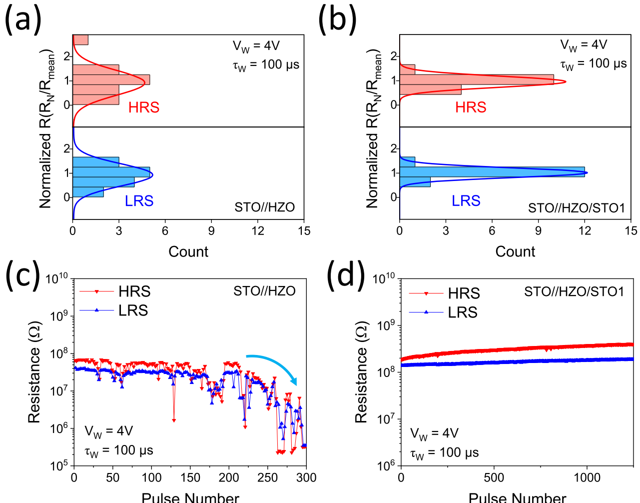

FIG. 4. (a) and (b) Distribution of the normalized LRS and HRS resistance values (R_N/R_{mean}) measured in a set of 15 junctions on STO//HZO and STO//HZO/STO1 samples, respectively. R_{mean} is the mean value of the {R_N} distribution. (c) and (d) Endurance of the representative junctions on STO//HZO and STO//HZO/STO1 samples, respectively, measured up to 300 writing/reading cycles for the STO//HZO sample and 1250 for the STO//HZO/STO1.

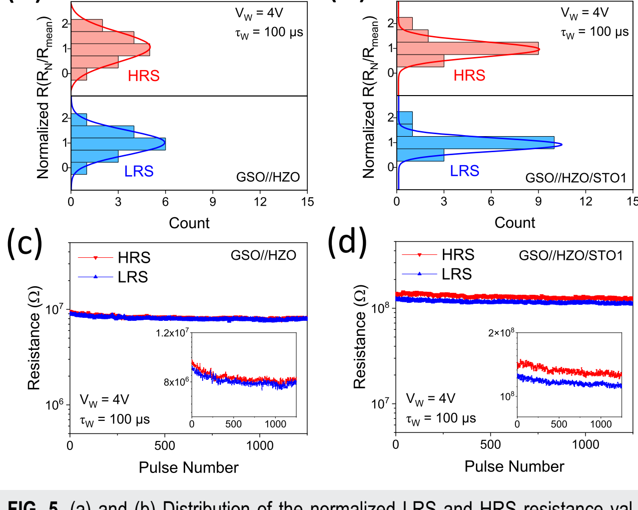

FIG. 5. (a) and (b) Distribution of the normalized LRS and HRS resistance values (R_N/R_{mean}) measured in a representative set of junctions on GSO//HZO and GSO//HZO/STO1 samples, respectively. (c) and (d) Endurance of the representative junctions on GSO//HZO and GSO//HZO/STO1 samples, respectively, measured up to 1250 writing/reading cycles. Data with zoomed-in view of scales are shown in the insets of (c) and (d).

is definitely enhanced as illustrated in Figs. 4(c) and 4(d). Indeed, the obvious degradation of the LRS/HRS states and their resistance contrast in the junctions on the bare STO//HZO [Fig. 4(c)] film is dramatically improved by the STO capping [Fig. 4(d)]. Note that in the STO//HZO/STO1 samples, the resistance increases while cycling, probably owing to the same mechanism that produces the increase in the resistance during device training. Similarly, as observed in Figs. 5(a) and 5(b), the spread of resistance values among different HZO junctions grown on GSO is also reduced by STO capping. The corresponding raw data are included in the supplementary material, S5. Instead, the endurance of junctions on GSO/HZO/STO1 [Fig. 5(d)] is similar to the uncapped GSO/HZO sample [not perceptible ER is observed in Fig. 5(c)].

Aiming at inspecting the electronic configuration of the atomic species at the surface of the bare STO//HZO and STO//HZO/STO1 and GSO//HZO and GSO//HZO/STO1 samples, we have collected the corresponding XPS spectra. To be able to probe different depths under the HZO surface, data have been collected at various emission angles θ ($\theta = 0°$, 45°, and 60°) with respect to the sample normal direction. In Figs. 6(a) and 6(b), we show the Hf-4f core level spectra of STO//HZO and STO//HZO/STO1 samples. The spin–orbit doublet dominates all spectra, with the Hf-4$f_{7/2}$ line at a binding energy (BE) BE = 17.58 eV, corresponding to Hf^{4+} in stoichiometric HfO_2 compounds.[24,25] The intensity of the Hf 4f lines in STO//HZO/STO is weaker than in the bare STO//HZO sample due to the attenuation of the escaping electrons at the upper STO capping layer. Therefore, to allow for a comparison of the shape of the XPS at different emission angles and on different samples, the measured intensity has been normalized to the maximum of the Hf-4$f_{7/2}$ line. The weak singlet visible at BE = 22.6 eV originates from O 2s core levels. Interestingly, in STO//HZO, the intensity of the O 2s line is clearly more pronounced at normal incidence than at oblique incidence, suggesting that the surface of STO//HZO is somehow oxygen depressed. Remarkably, in STO//HZO/STO1 [Fig. 6(b)], this angular emission dependence of the O 2s line disappears, and the explored sample depth appears to be homogeneous in its oxygen contents. To what extent this change reflects a modification (enrichment) of oxygen concentration in the top layers of HZO in the capped sample or simply results from the additional contribution of the O 2s signal from the STO capping cannot be discriminated by these experiments.

On the other hand, the inspection of the lower binding energy edge of Hf 4f is interesting, as the possible presence of reduced Hf species, such as Hf^{3+}, could lead to the emergence of the corresponding core levels, as observed in HfO_{2-x}.[26] Data in Figs. 6(a) and 6(b) show the XPS Hf-4f spectra of the bare HZO film and HZO/STO films. The vertical dashed lines indicate the expected positions of Hf^{4+} and Hf^{3+} lines. A comparison of data in Figs. 6(a) and 6(b) reveals a tiny but perceptible difference in the low energy tail, where the position of Hf^{3+} is expected, which is definitely more pronounced in the capped sample. The Hf-4f core level XPS spectra of GSO//HZO and GSO//HZO/STO show smaller differences (see the supplementary material, S6). Moreover, angular emission dependent data in Fig. 6(b) suggest that the Hf^{3+} contribution to the tail is more pronounced when approaching grazing incidence. This can be clearly appreciated in Figs. 6(d)–6(f), where the deconvolution of the XPS lines into Hf^{4+} and Hf^{3+} (and O-2s) lines is indicated. The observed Hf^{3+}/Hf^{4+} variation implies a richer Hf^{3+} fraction at the HZO/STO interface. Consequently, the interface would be more reduced, maybe due to oxygen scavenging by the grown STO layer (Hf^{3+} contribution quantification is included in the supplementary material, S7).

© Author(s) 2022

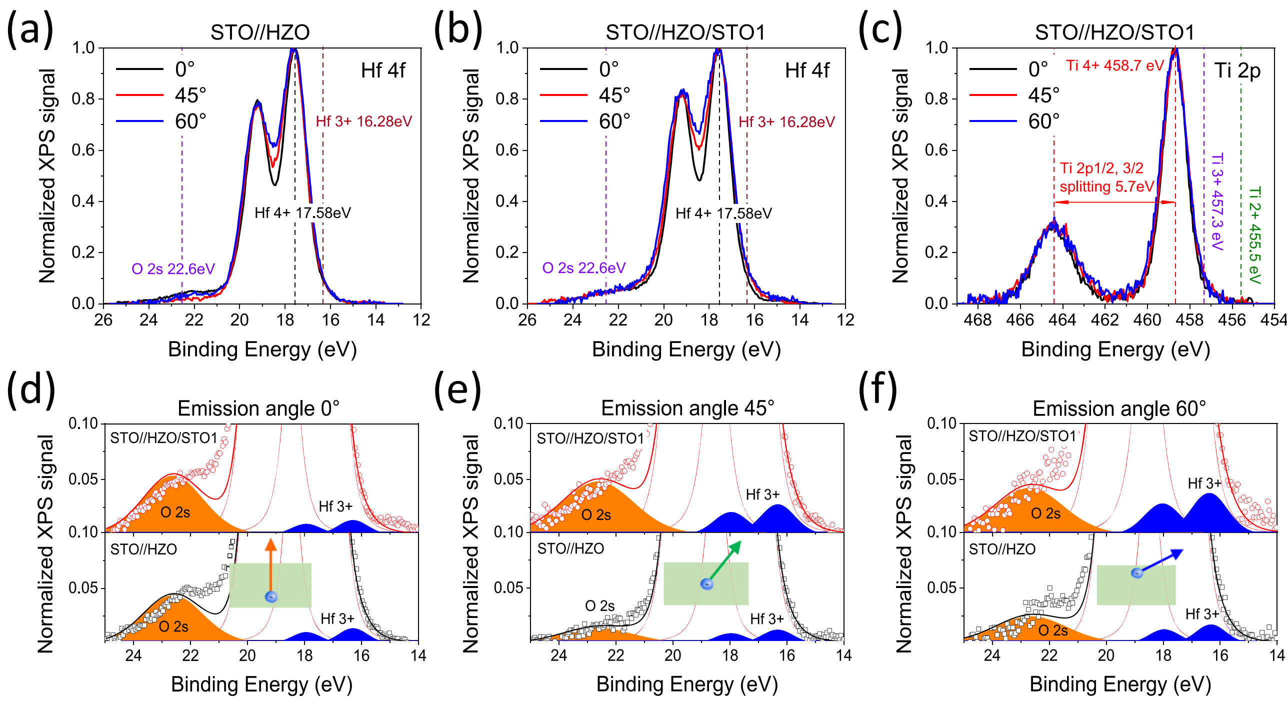

FIG. 6. XPS Hf 4f core spectra of STO//HZO (a) and STO//HZO/STO1 (b) samples recorded at various emission angles. The vertical dashed lines indicate the expected positions of the Hf-$4f_{7/2}$ line of Hf^{4+} and Hf^{3+} and the position of the O 2s line. (c) XPS Ti 2p spectra collected at various emission angles. The vertical dashed lines indicate the expected positions of the Hf-$4f_{7/2}$ line of Hf^{4+} and Hf^{3+} and the position of the O 2s line. (d)–(f) Zoomed-in view of the XPS spectra recorded at different emission angles, with the deconvolution of Hf^{4+} and Hf^{3+} (blue areas) and O 2s (orange area) lines for STO//HZO (bottom panels) and STO//HZO/STO1 (top panels) samples.

The Ti 2p spectra of the capping STO layer have also been recorded at various emission angles [Fig. 6(c)]. The Ti 2p spectra displays the spin–orbit doublet $2p_{3/2}$ and $2p_{1/2}$, where the EB($2p_{3/2}$) = 458.7 eV is characteristic of Ti^{4+}, and the data recorded at various emission angles are coincident. No features suggesting the presence of Ti^{3+} can be detected at any emission angle. The Ti 2p spectra of the STO capping layer are also virtually indistinguishable from those of the bare STO substrates. At this point, it is pertinent to recall that the earlier electron energy loss spectrum (EELS) recorded on (thickness of 4.5 nm) HZO films capped with STO suggested the presence of Ti^{3+} reduced species at the capping layer,[16] which are not visible in the XPS data of the present HZO/STO heterostructure. In any event, as shown in the following, the capping layer has the benefit of producing a conformal coating of the HZO layer.

The high spatial resolution provided by aberration corrected scanning transmission electron microscopy (STEM) allows us to observe the conformal covering of the HZO film by the 1 nm-thick STO capping film. Figure 7(a) shows a cross-sectional high angle annular dark field (HAADF) image where the LSMO bottom electrode (grown on STO), the HZO film, the STO (1 nm) capping film, and the Pt top electrode can be observed from the bottom to the top of the image. In particular, the conformal covering of HZO by the STO(1 nm) layer becomes evident by superimposing the Ti L-edge chemical map integrated from the corresponding electron energy loss spectrum (EELS) to the HAADF image, as shown in the right

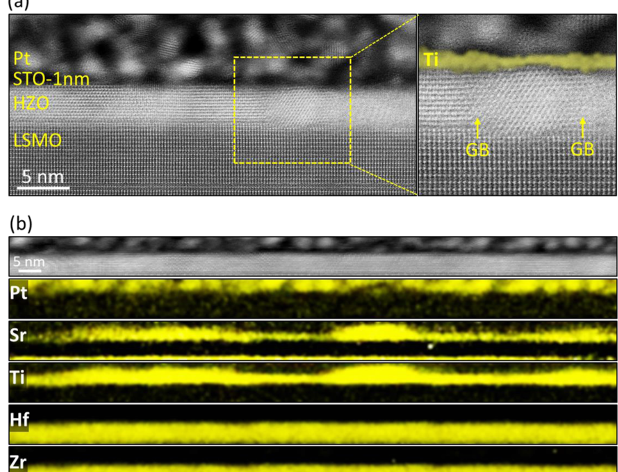

FIG. 7. (a) STO//HZO/STO1 film. A HAADF image of the LSMO bottom electrode, the HZO film, the STO-1 nm capping film, and the Pt top electrode. In order to clearly image the conformal covering of the HZO film by STO, the right side inset shows an enlarged region with the corresponding Ti L-edge chemical map (in faded yellow) from EELS superimposed onto the HAADF image. The location of the grain boundaries (GBs) is marked with yellow arrows. (b) From the top to the bottom, the HAADF image, Pt, Sr, Ti, Hf, and Zr chemical maps corresponding to a larger horizontal area than the one shown in (a).

© Author(s) 2022

side inset of Fig. 7(a). Note that the STO capping layer conformably covers the boundaries between the grains (GBs) in the HZO film. Further proof of the high-quality of the stack is provided in Fig. 7(b), where the HAADF image and the corresponding Pt–M, Sr–L, Ti–L, Hf–M, and Zr–L EELS chemical maps of a wider horizontal area are shown. The image resolution does not allow us to disclose the crystalline state of the top STO layer. However, STEM images of similar capping on relatively thicker HZO films (4.8 nm) grown under nominally identical conditions allowed us to observe the crystalline nature of the STO capping layer.[16] Therefore, it is likely that the top STO layer here, in addition to being conformally covering the HZO, is also crystalline. Note that in the capped samples, the interface (STO/Pt) should be different than for the uncapped (HZO/Pt) due to defect chemistry, electronic reconstructions, and/or band alignments. Available data, including EELS and STEM, do not allow addressing this issue.

CONCLUSIONS

In summary, we have shown that relatively large capacitors (diameter of 20 μm) prepared on epitaxial ultrathin films of HZO, only ≈2.2 nm thick, grown on single crystalline STO and GSO substrates display a pronounced ER that exceeds 150% at room temperature. Capping these ultrathin films with a dielectric layer (here, STO) of about 1 nm increases the junction resistance. Importantly, the STO capping layer allows us to obtain a higher junction yield in a given sample and a reduction in the spread of the obtained resistance values. Moreover, the endurance of HZO in both structures is clearly enhanced. The picture that emerges is that the capping layer primarily blocks conducting channels across the grain boundaries that exist in the film due to either the presence of different variants of the ferroelectric o-phase or the spurious m-phase, and promotes a higher fraction of reduced species near the top HZO/STO interface region, as observed by XPS. In polycrystalline films, a larger abundance of grain boundaries is to be expected and consequently, a similar strategy can help to mitigate their detrimental contribution to ER and to improve the device performance, crucial for applications.

SUPPLEMENTARY MATERIAL

See the supplementary material for additional piezoelectric force microscopy, XPS, and electrical characterization data.

ACKNOWLEDGMENTS

Financial support from the Spanish Ministry of Science and Innovation (MCIN/AEI/10.13039/501100011033) through the Severo Ochoa FUNFUTURE (Grant No. CEX2019-000917-S) and Grant Nos. PID2019-107727RB-I00, PID2020-112548RB-I00, and PID2020-118479RB-I00; the Consejo Superior de Investigaciones Científicas through i-LINK (Grant No. LINKA20338) program; and the Generalitat de Catalunya (Grant No. 2017 SGR 1377) are acknowledged. This project was supported by a 2020 Leonardo Grant for Researchers and Cultural Creators, BBVA Foundation. Xiao Long and Huan Tan are financially supported by the China Scholarship Council (CSC) under Grant Nos. 201806100207 and 201906050014. The work of Xiao Long and Huan Tan was done as a part of their Ph.D. program in Materials Science at Universitat Autònoma de Barcelona. Saúl Estandía acknowledges the Spanish Ministry of Economy, Competitiveness and Universities for his Ph.D. Contract (No. SEV-2015-0496-16-3) and its cofunding by the ESF.

AUTHOR DECLARATIONS

Conflict of Interest

The authors declare no conflict of interest.

DATA AVAILABILITY

The data that support the findings of this study are available within the article and its supplementary material.

REFERENCES

[1] M. H. Park *et al.*, J. Mater. Chem. C **5**, 4677 (2017).
[2] U. Schroeder *et al.*, Jpn. J. Appl. Phys. **53**, 08LE02 (2014).
[3] M. H. Park *et al.*, Adv. Mater. **27**, 1811 (2015).
[4] R. Materlik *et al.*, J. Appl. Phys. **117**, 134109 (2015).
[5] S. Estandía *et al.*, J. Mater. Chem. C **9**, 3486 (2021).
[6] G. Bersuker *et al.*, J. Appl. Phys. **110**, 124518 (2011).
[7] B. Max *et al.*, J. Appl. Phys. **123**, 134102 (2018).
[8] K. McKenna and A. Shluger, Appl. Phys. Lett. **95**, 222111 (2009).
[9] K.-H. Xue *et al.*, Appl. Phys. Lett. **102**, 201908 (2013).
[10] G. Bersuker *et al.*, Solid State Electron. **65–66**, 146 (2011).
[11] M. Lanza *et al.*, Appl. Phys. Lett. **101**, 193502 (2012).
[12] M. Lanza *et al.*, Appl. Phys. Lett. **100**, 123508 (2012).
[13] P. Calka *et al.*, Nanotechnology **24**, 085706 (2013).
[14] S. Estandía *et al.*, ACS Appl. Electron. Mater. **1**, 1449 (2019).
[15] M. C. Sulzbach *et al.*, Adv. Electron. Mater. **6**, 1900852 (2019).
[16] M. C. Sulzbach *et al.*, Adv. Funct. Mater. **30**, 2002638 (2020).
[17] M. Cervo Sulzbach *et al.*, ACS Appl. Electron. Mater. **3**, 3657 (2021).
[18] J. Lyu *et al.*, Appl. Phys. Lett. **113**, 082902 (2018).
[19] P. D. Nellist and S. J. Pennycook, Ultramicroscopy **78**, 111 (1999).
[20] F. Ambriz-Vargas *et al.*, ACS Appl. Mater. Interfaces **9**, 13262 (2017).
[21] F. Ambriz-Vargas *et al.*, Appl. Phys. Lett. **110**, 093106 (2017).
[22] B. Prasad *et al.*, Adv. Electron. Mater. **7**, 2001074 (2021).
[23] Y. Goh *et al.*, Appl. Phys. Lett. **117**, 242901 (2020).
[24] A. Chernikova *et al.*, ACS Appl. Mater. Interfaces **8**, 7232 (2016).
[25] W. Hamouda *et al.*, J. Appl. Phys. **127**, 064105 (2020).
[26] L. Porte *et al.*, Phys. Rev. B **28**, 3214 (1983).

© Author(s) 2022